Electronic Supplementary Material (ESI) for Journal of Materials Chemistry A.


# *Supporting Information*

# Trends in the phase stability and thermochemical oxygen exchange of ceria doped with potentially tetravalent metals

Roger Jacot, René Moré, Ronald Michalsky, Aldo Steinfeld, and Greta R. Patzke*

## Table of Contents

**Experimental data**

***Parameters for ICP-MS measurements:*** Samples were investigated with a feed of 0.3 mL/min and an RF power of 1550 W. Tune settings were based on the Agilent General Purpose method and only slightly modified by an auto tune procedure using an Agilent 1 ppb tuning solution containing Li, Y, Ce, and Tl. Values are reported as the average of 30 sweeps x 3 replicates. Elements were measured in a "nogas" mode, where the instrument is set to a single quadrupole setting. In addition, they were also determined in a "helium-mode" and an "oxygen-mode" for additional information. The names are referring to the gases in the reaction cell. Elements in the "oxygen-mode" were measured as their oxides $MO^+$ with an e/z mass plus 16. For example, cerium (e/z = 140) was detected as mass 156 ($CeO^+$ with e/z = 156) instead. All solutions were prepared from 60% $HNO_3$ (Merck 1.1518.1000 ultrapur), HCl (Fluka 1.00316.2500) and/or >= 18.2 MΩ Millipore water. Elements were measured against a serial dilution made with the following standards:

Niobium: Merck 1.70337.0100 in water

Hafnium: Merck 1.70322.0100 in 7% HCl

Zirconium: Merck 1.70390.0100 in 7% HCl

Chromium: Merck 1.70312.0100 in 2% $HNO_3$

Vanadium: Merck 1.70366.0100 in 2% $HNO_3$

Cerium: Agilent 8500-60372 Multielement standard in 2% $HNO_3$

Praseodymium: Agilent 8500-60372 Multielement standard in 2% $HNO_3$

Terbium: Agilent 8500-60372 Multielement standard in 2% $HNO_3$

Indium: Merck 1.70324.0100 in 2% $HNO_3$ as internal standard

Samples were dissolved in 1 mL conc. aqua regia with the addition of some fluoride (addition of 200 microliters of a 1 m aqueous $NH_4F$ solution (made from Merck 1.01164.0250 and Millipore-water) and diluted to 10 mL with Millipore water. This stock solution was adjusted for a ≈2% aqua regia concentration by a subsequent dilution with 2% aqua regia.

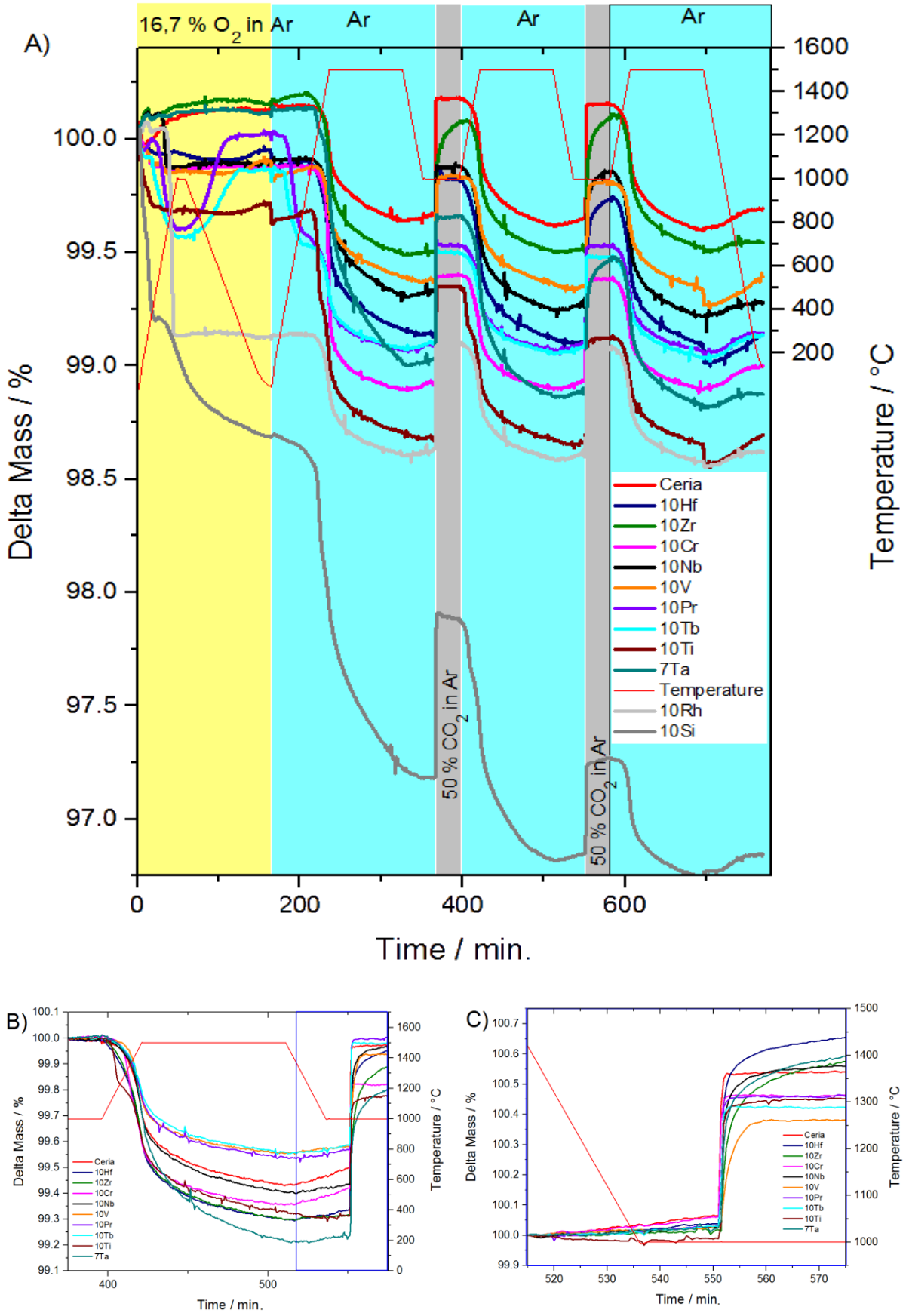


**Figure S1.** (a) Overview of 2.5 TGA cycles with all thermally stable doped ceria samples, (b) reduction step of the second TGA cycle, (c) oxidation step of the second TGA cycle.

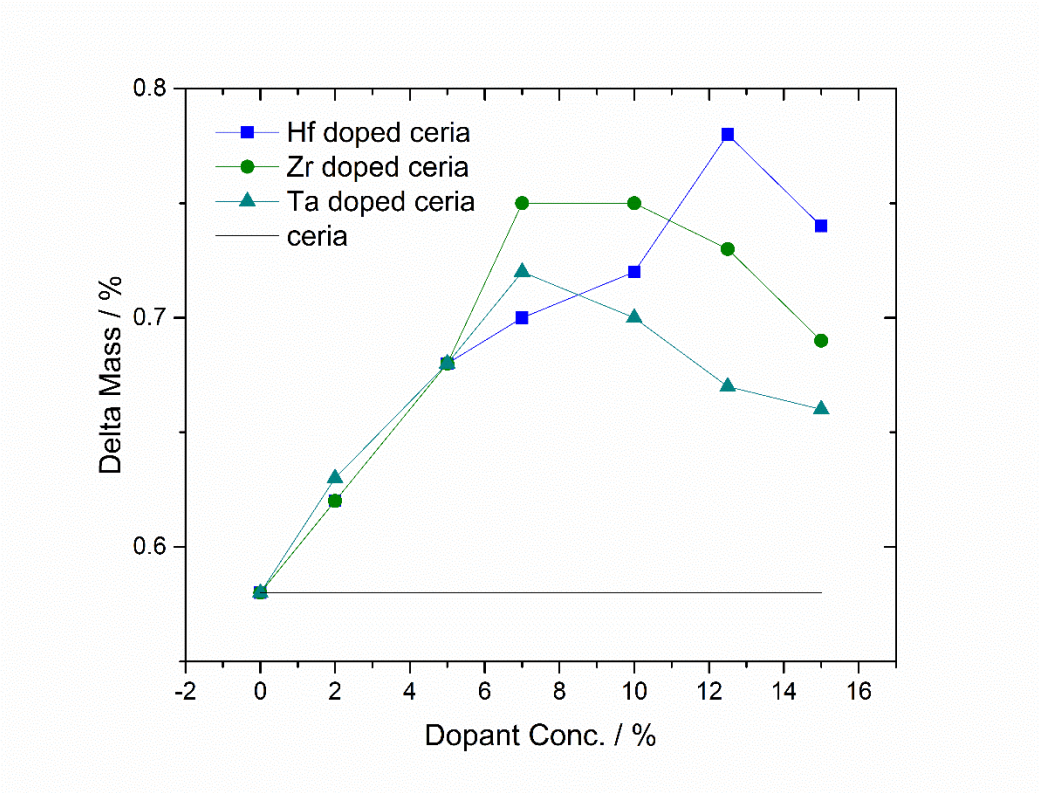


**Figure S2.** Mass change during the second TGA cycle with different dopant concentrations of Cr, Nb, Hf, Zr, and Ta.

To determine the optimal working point for dopant concentration in ceria, $M_xCe_{1-x}O_2$ samples (M = Hf, Zr, and Ta; x = 0.02, 0.05, 0.07 and 0.1) were synthesized and compared to pristine ceria with TGA cycling experiments.

Figure S2 displays a plateau for the oxygen exchange capacity around 10% ± 2.5 % dopant concentrations in TGA cycling experiments.

The working point for the general dopant concentration in the present study was finally selected as 10 metal% for the sake of consistency, because most dopants led to a signficant OEC enhancement of ceria around this concentration. One exception was made for Ta, where the working concentration was adjusted somewhat lower (around 7 metal%).

Furthermore, previous studies reported optimal ionic conductivities of doped ceria for this range,[1] and the OEC is likely to be linked to the ionic mobilities in doped ceria.

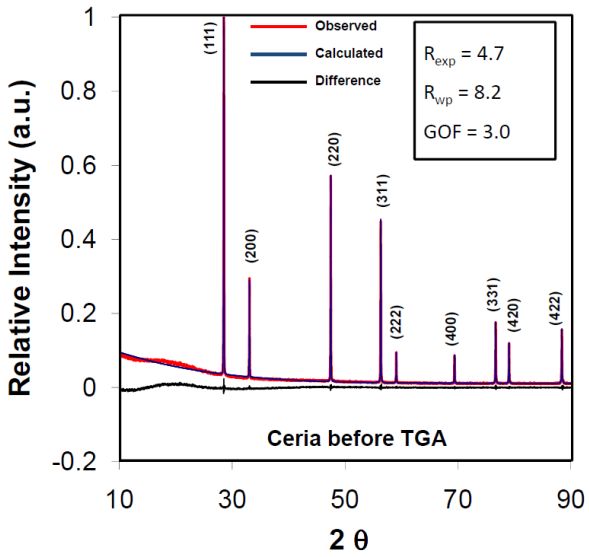
Observed
Calculated
Difference
$R_{exp}$ = 4.7
$R_{wp}$ = 8.2
GOF = 3.0
(111)
(200)
(220)
(311)
(222)
(400)
(331)
(420)
(422)
Ceria before TGA
Relative Intensity (a.u.)
2 θ

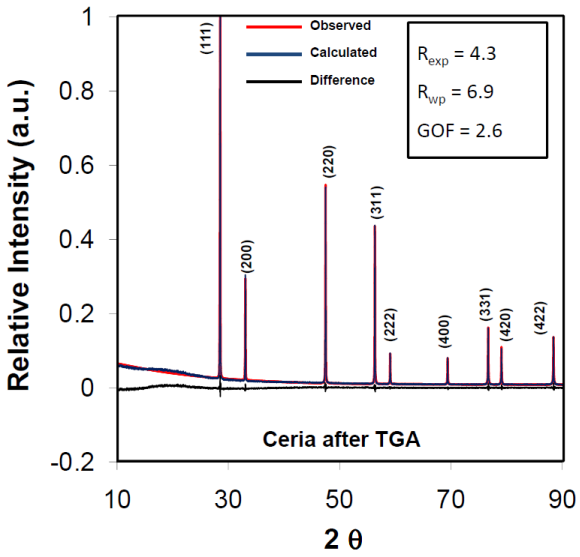
Observed
Calculated
Difference
$R_{exp}$ = 4.3
$R_{wp}$ = 6.9
GOF = 2.6
(111)
(200)
(220)
(311)
(222)
(400)
(331)
(420)
(422)
Ceria after TGA
Relative Intensity (a.u.)
2 θ

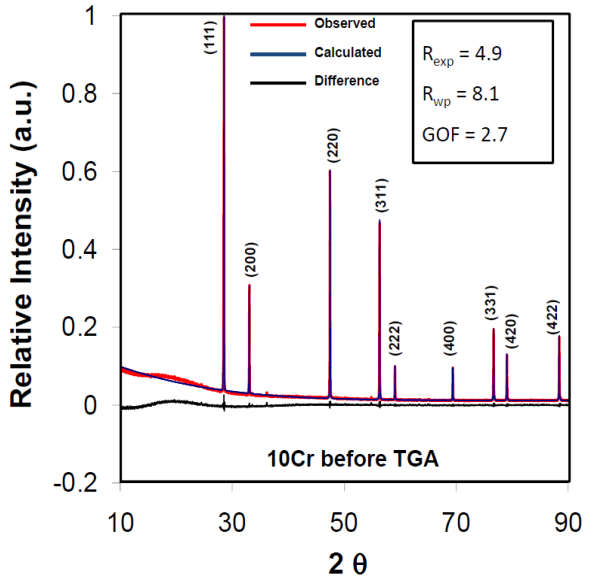
Observed
Calculated
Difference
$R_{exp}$ = 4.9
$R_{wp}$ = 8.1
GOF = 2.7
(111)
(200)
(220)
(311)
(222)
(400)
(331)
(420)
(422)
10Cr before TGA
Relative Intensity (a.u.)
2 θ

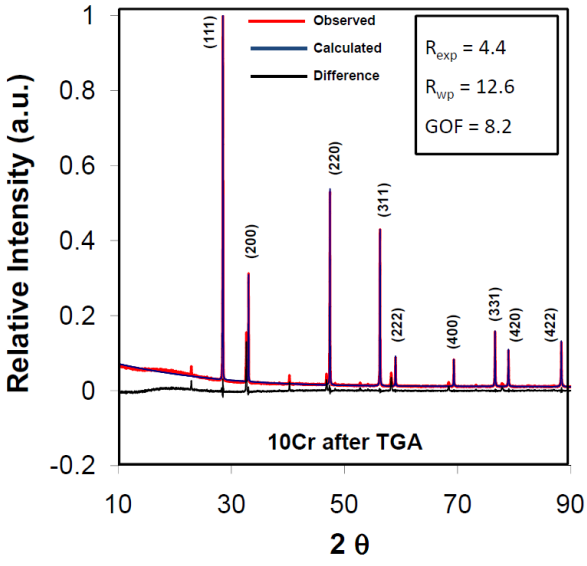
Observed
Calculated
Difference
$R_{exp}$ = 4.4
$R_{wp}$ = 12.6
GOF = 8.2
(111)
(200)
(220)
(311)
(222)
(400)
(331)
(420)
(422)
10Cr after TGA
Relative Intensity (a.u.)
2 θ

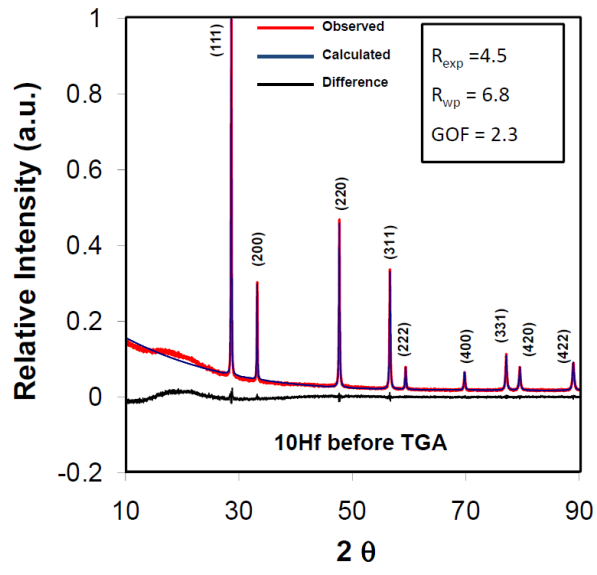
Observed
Calculated
Difference
$R_{exp}$ =4.5
$R_{wp}$ = 6.8
GOF = 2.3
(111)
(200)
(220)
(311)
(222)
(400)
(331)
(420)
(422)
10Hf before TGA
Relative Intensity (a.u.)
2 θ

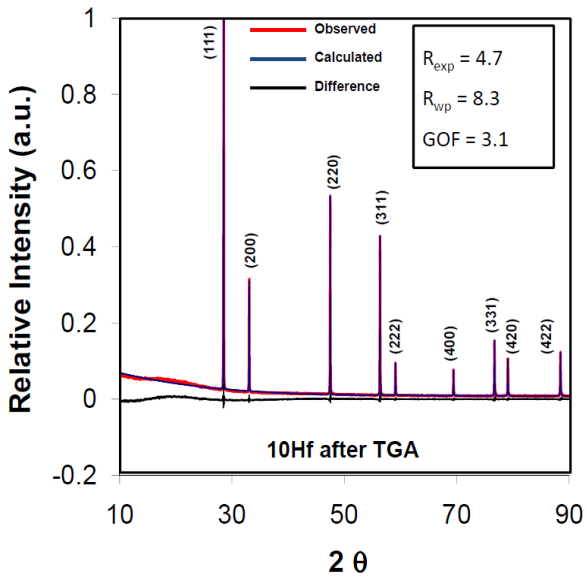
Observed
Calculated
Difference
$R_{exp}$ = 4.7
$R_{wp}$ = 8.3
GOF = 3.1
(111)
(200)
(220)
(311)
(222)
(400)
(331)
(420)
(422)
10Hf after TGA
Relative Intensity (a.u.)
2 θ

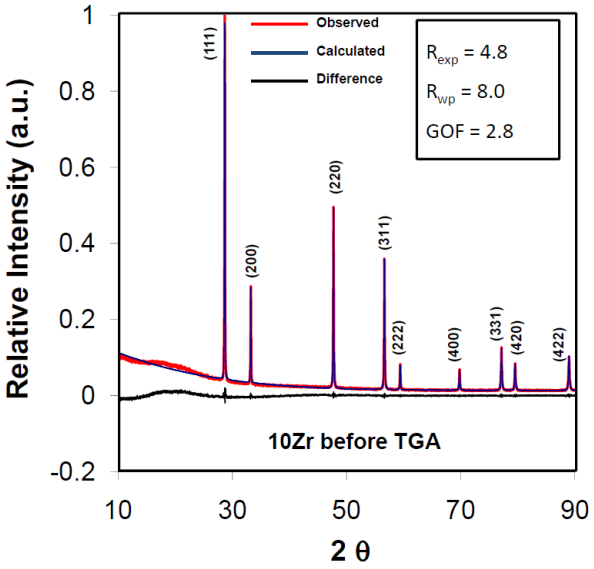
Observed
Calculated
Difference
$R_{exp}$ = 4.8
$R_{wp}$ = 8.0
GOF = 2.8
(111)
(200)
(220)
(311)
(222)
(400)
(331)
(420)
(422)
10Zr before TGA
Relative Intensity (a.u.)
2 θ

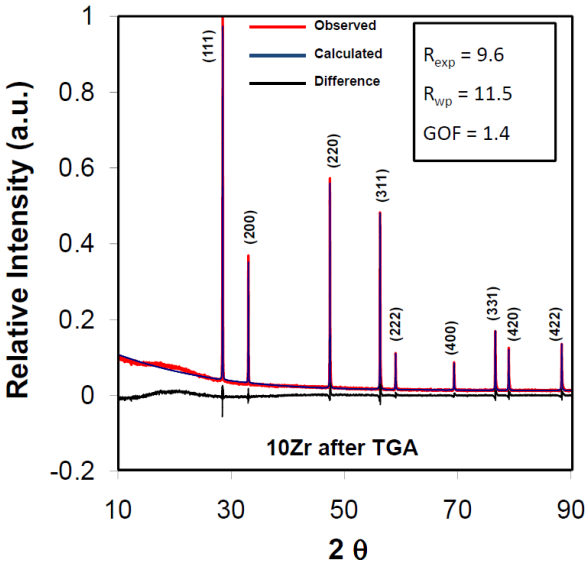
Observed
Calculated
Difference
$R_{exp}$ = 9.6
$R_{wp}$ = 11.5
GOF = 1.4
(111)
(200)
(220)
(311)
(222)
(400)
(331)
(420)
(422)
10Zr after TGA
Relative Intensity (a.u.)
2 θ

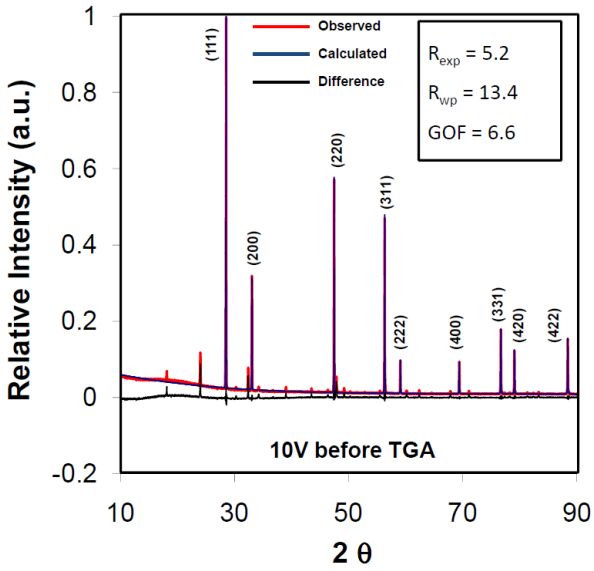
Observed
Calculated
Difference
$R_{exp}$ = 5.2
$R_{wp}$ = 13.4
GOF = 6.6
(111)
(200)
(220)
(311)
(222)
(400)
(331)
(420)
(422)
10V before TGA
Relative Intensity (a.u.)
2 θ

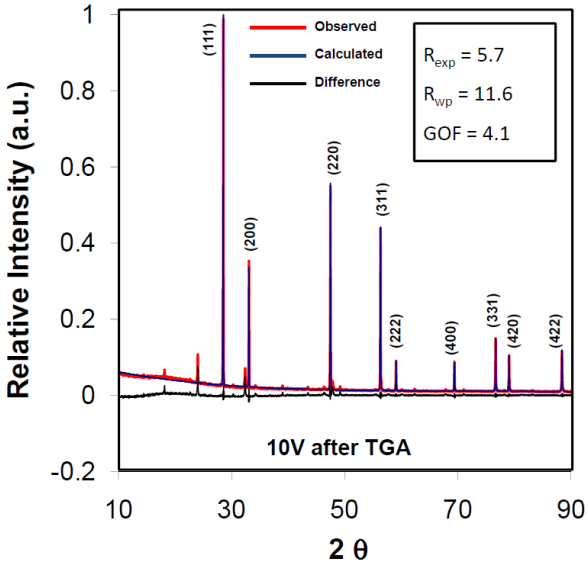
Observed
Calculated
Difference
$R_{exp}$ = 5.7
$R_{wp}$ = 11.6
GOF = 4.1
(111)
(200)
(220)
(311)
(222)
(400)
(331)
(420)
(422)
10V after TGA
Relative Intensity (a.u.)
2 θ

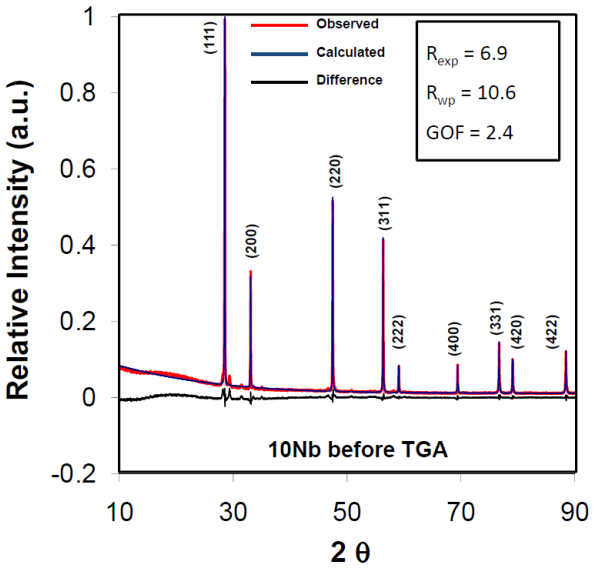
Observed
Calculated
Difference
$R_{exp}$ = 6.9
$R_{wp}$ = 10.6
GOF = 2.4
(111)
(200)
(220)
(311)
(222)
(400)
(331)
(420)
(422)
10Nb before TGA
Relative Intensity (a.u.)
2 θ

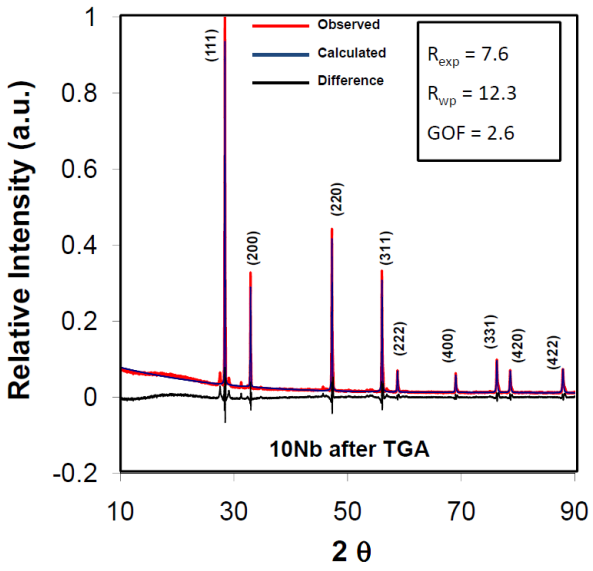
Observed
Calculated
Difference
$R_{exp}$ = 7.6
$R_{wp}$ = 12.3
GOF = 2.6
(111)
(200)
(220)
(311)
(222)
(400)
(331)
(420)
(422)
10Nb after TGA
Relative Intensity (a.u.)
2 θ

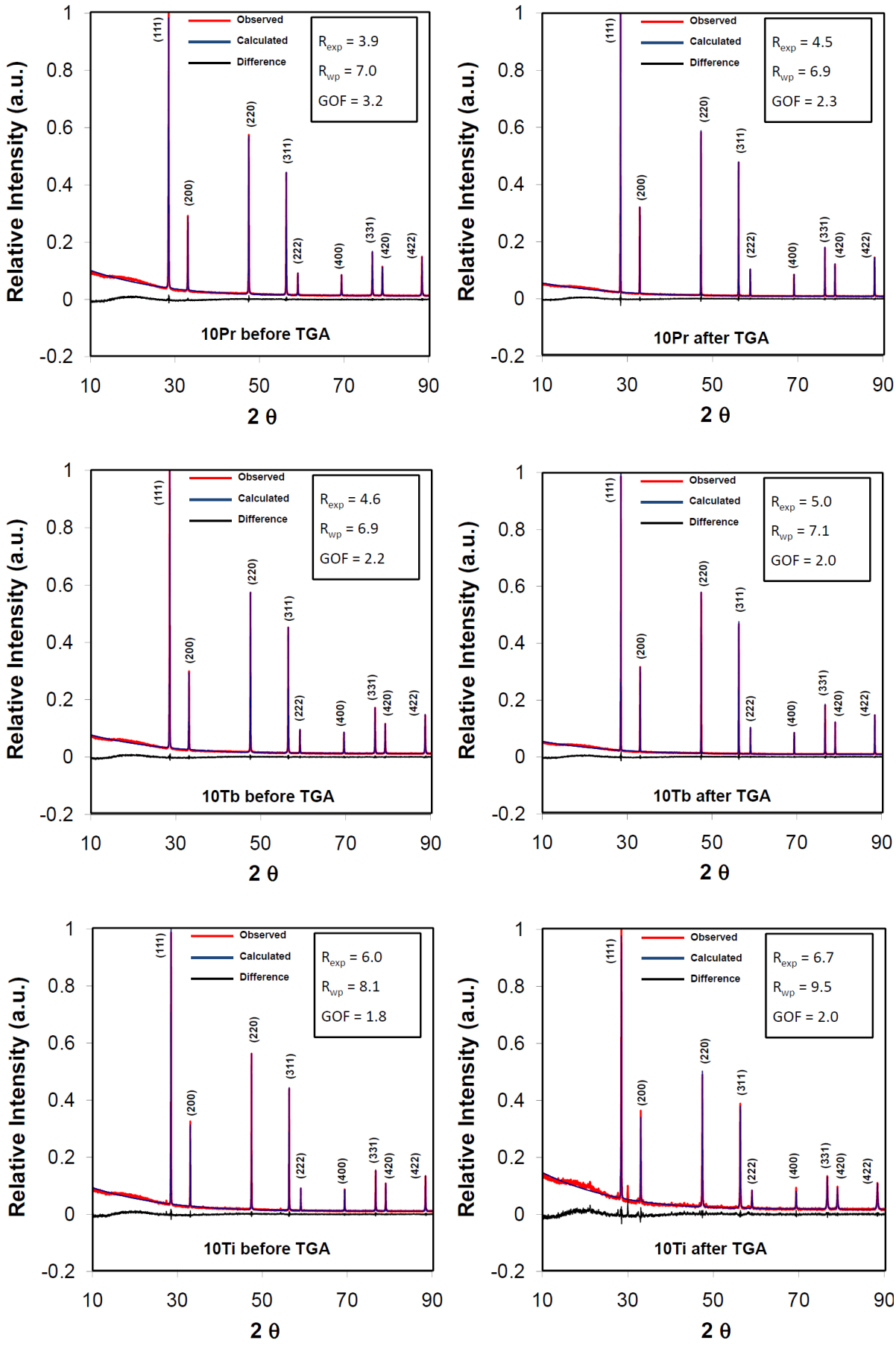
Observed
Calculated
Difference
$R_{exp}$ = 3.9
$R_{wp}$ = 7.0
GOF = 3.2
10Pr before TGA
$R_{exp}$ = 4.5
$R_{wp}$ = 6.9
GOF = 2.3
10Pr after TGA
$R_{exp}$ = 4.6
$R_{wp}$ = 6.9
GOF = 2.2
10Tb before TGA
$R_{exp}$ = 5.0
$R_{wp}$ = 7.1
GOF = 2.0
10Tb after TGA
$R_{exp}$ = 6.0
$R_{wp}$ = 8.1
GOF = 1.8
10Ti before TGA
$R_{exp}$ = 6.7
$R_{wp}$ = 9.5
GOF = 2.0
10Ti after TGA
(111)
(200)
(220)
(311)
(222)
(400)
(331)
(420)
(422)
Relative Intensity (a.u.)
2 θ

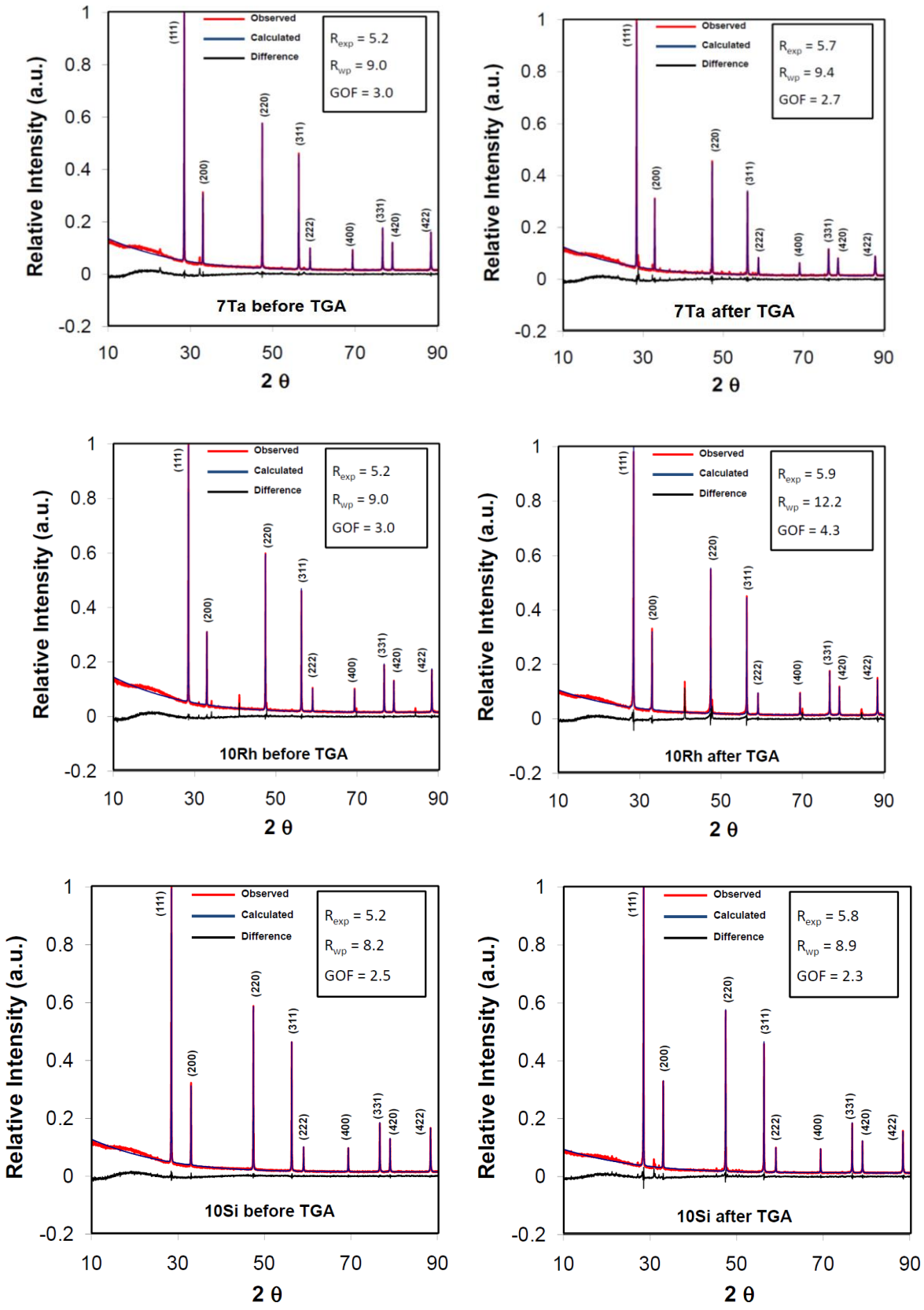


**Figure S3.** Rietveld refinement of PXRD patterns recorded on pristine and doped ceria samples before and after TGA. Rietveld refinements were performed with the JANA 2006 software package.[2]

When comparing the GOF (goodness of fit) values [$(R_{wp} / R_{exp})^2$] and the difference plots in Fig. S3 it is obvious that the quality of the Rietveld refinements varies widely. Especially the fits for PXRD patterns with more than one phase display high GOF- and R-values. We thus refrained from applying Vegard's law in the present study.

Note that Rietveld refinements with a GOF value above 3 (e.g. 10Hf after TGA) can still be of acceptable quality[3] when it is taken into account that the selected background model was less appropriate for lower angles. In these cases, the difference plot is a more reliable criterion, so that we present the Rietveld refinements of 10Hf before/after TGA, 10Zr before TGA, 10Pr and Tb before/after TGA, and 10Si before TGA along with the other data.

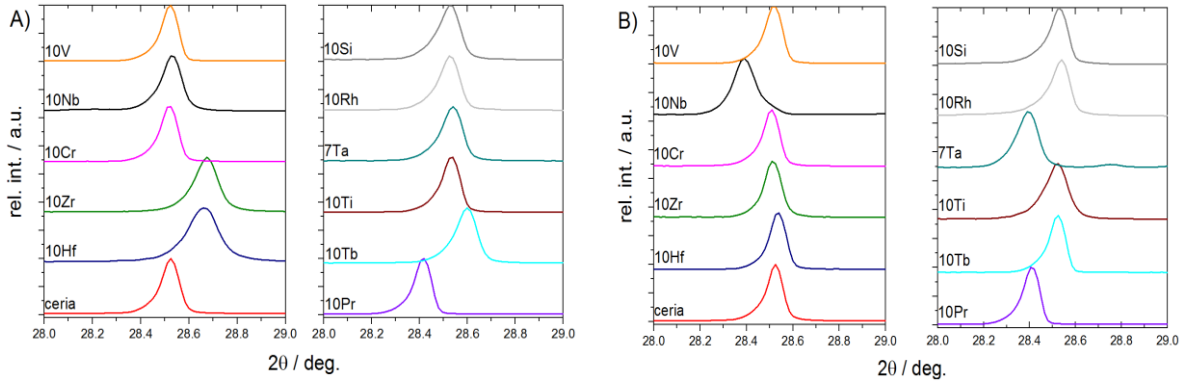


**Figure S4.** Zoom into the region between 28 and 29 ° for PXRD patterns of doped ceria samples before (a) and after (b) TGA.

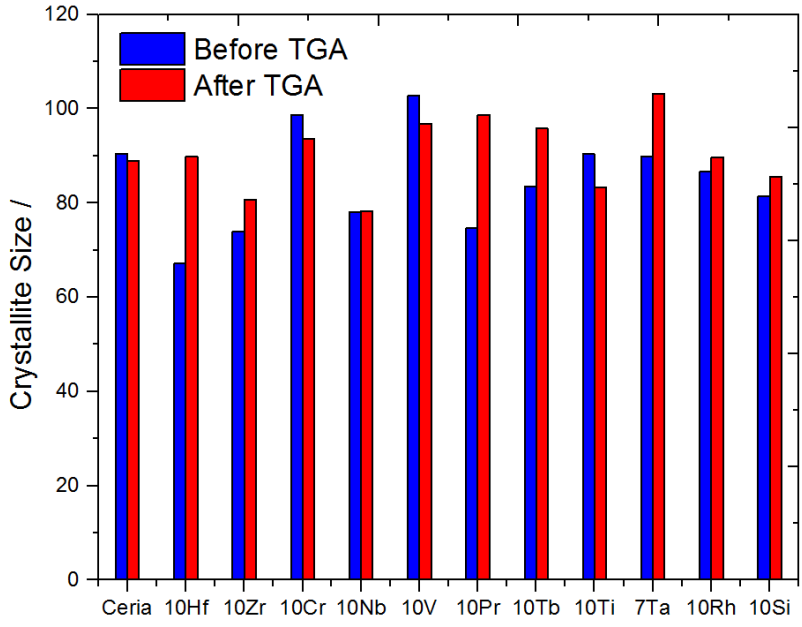


**Figure S5.** Crystallite size before and after TGA determined from the Scherrer equation (Eq. 1).

Parameters for the Scherrer equation:

$$D_{XRD} = \frac{K * \lambda}{\beta * cos(\theta)} \quad (1)$$

$D_{XRD}$ = crystallite size

$K$ = form factor for cubic shape = 0.94

$\lambda_{CuK\alpha}$ = X-ray wavelength = 1.54051 * $10^{-10}$ m

$\beta$ = full width at half maximum (FWHM) in radian

$\theta$ = Bragg angle

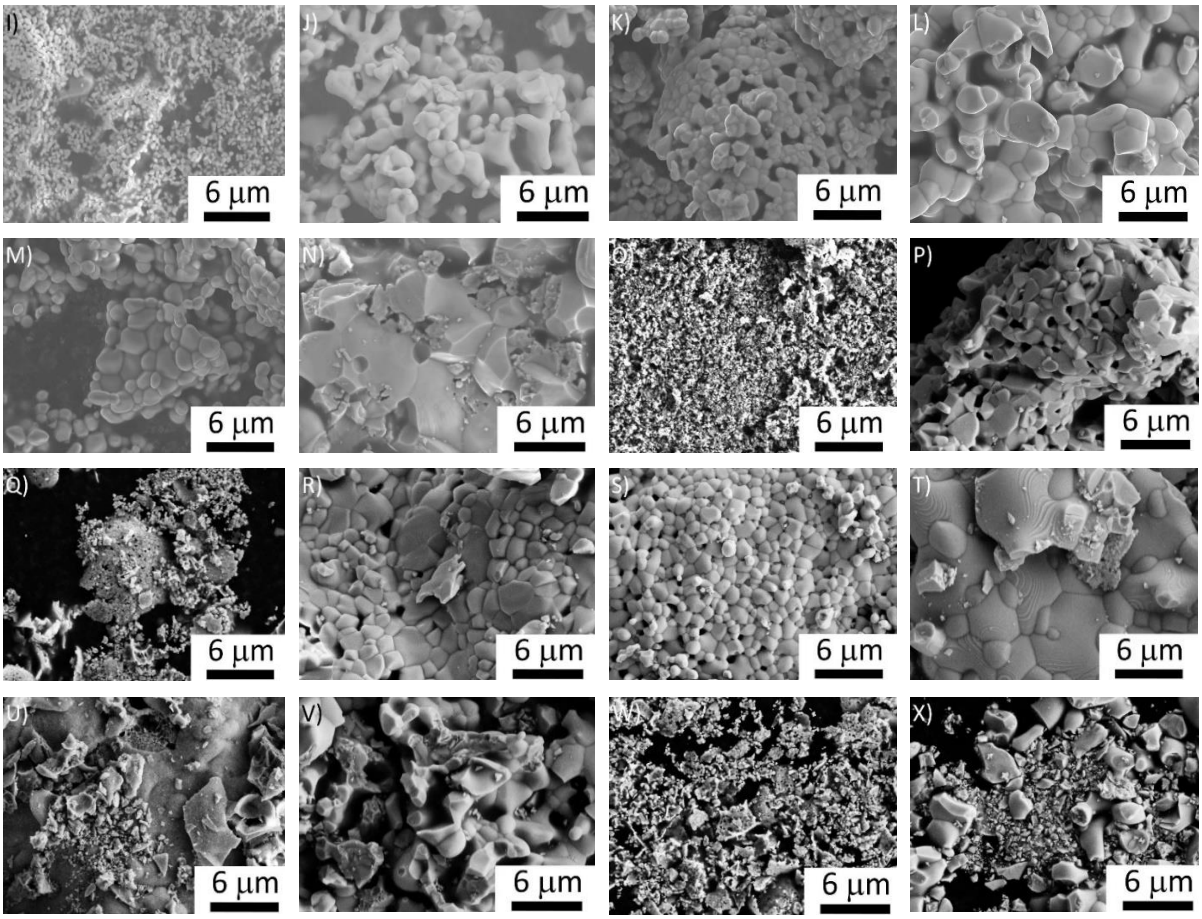


**Figure S6.** Representative SEM images of selected samples before (left) and after TGA (right; continued from the main text) of 10Cr (i, j), 10Nb (k, l), 10V (m, n), 10Pr (o, p), 10Tb (q, r), 10Ti (s, t), 10Si (u, v), and 10Rh (w, x).

**Detailed evaluation of UV/Vis spectroscopy results for doped ceria samples**

All doped ceria samples undergo a color change after TGA cycling experiments, mainly from pale yellow to grey (or from light to dark red-brown for 10Ti, 10Pr, and 10Tb, respectively) due to the formation of reduced ceria or lanthanide centers. The brownish color of Pr-doped ceria has been assigned to $Ce^{4+}$ - $Pr^{3+}$ transitions.[1] The characteristic $Ce^{4+} \leftarrow O^{2-}$ charge transfer bands (285 nm) and interband transitions (340 nm) of pure ceria were observed for all doped samples in the 265 - 275 nm range and around 349 nm before and after TGA investigations (Figure S7). While the bands around 275 nm are rather weak plateaus, the transition around 349 nm displays red shifts of about 10 - 20 nm for 10Ti, 10Zr, 10Hf, 10V, and 10Nb before TGA and around 10 nm for all samples after TGA. An additional $Ce^{3+} \leftarrow O^{2-}$ charge transfer band around 255 nm[4] or 265 nm[5] is present in all samples, except for 10Si, 10Rh, 7Ta, and ceria (277 nm before TGA and 260 nm after TGA). As the spectra were recorded in reflectance mode, their intensities after TGA treatment were generally diminished due to the darker sample colors which render the evaluation of the band gap energies of 10Pr, 10Tb, 10Nb, and 10V before and after TGA impossible. Additionally, the dark color appearing after TGA makes the determination of the band gap energy quite difficult.

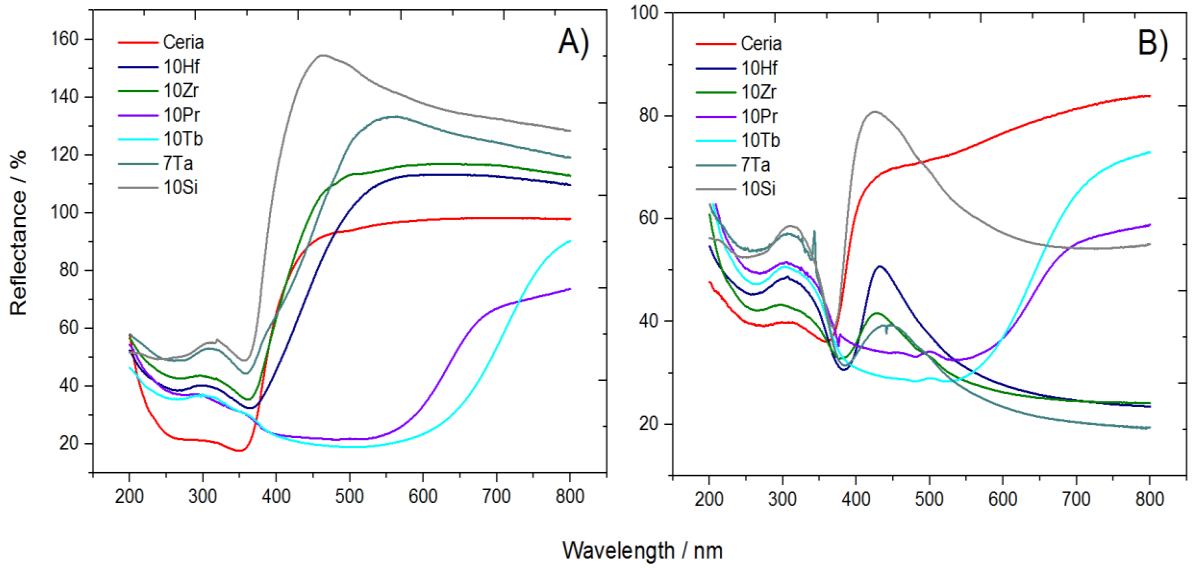


**Figure S7.** UV/Vis spectra of doped ceria before (a) and after (b) TGA. Spectra of the following strongly absorbing samples are not shown for clarity:10V, 10Nb, 10Rh, 10Ti and 10Cr.

**Detailed evaluation of FT-IR spectroscopy results for doped ceria samples**

All FT-IR spectra were checked for characteristic hydrogen carbonate and carbonate bands (values from ref. 6). Monodentate carbonate (1504 $cm^{-1}$) could be excluded as well as bidentate (1567 $cm^{-1}$, 1289 $cm^{-1}$, and 1014 $cm^{-1}$) and polydentate carbonate (1351 $cm^{-1}$) species. Only 10Tb and 10Cr display traces of bridged and hydrogen carbonate bands around 1125 $cm^{-1}$ and 1150 $cm^{-1}$ prior to TGA, while the 2127 $cm^{-1}$ band of trapped CO could not be detected at all.

The three characteristic bands of pure ceria[5] are a significant ν(CeO) mode at 730 $cm^{-1}$, a fundamental vibration mode at 530 $cm^{-1}$ and its first overtone at 1025 $cm^{-1}$. In line with previous work,[7] the band at 530 $cm^{-1}$ could not be observed in all spectra and the 1025 $cm^{-1}$ vibration was only very weak. Additional peaks in the region around 600 to 1200 $cm^{-1}$ are only present in biphasic samples. The most characteristic band of all ceria samples was observed around 720 $cm^{-1}$ (with some shifts) after 2.5 cycles of TGA treatment, except for 10Hf and 10Zr. Generally, the intensity of this vibration decreased somewhat after TGA treatment, hand in hand with a shift towards lower wavenumbers. 10Cr, 10Nb, 10Ti, and 7Ta before and after TGA exhibit significant shifts towards lower wavenumbers, while the respective band of 10V is shifted into the opposite direction. The band shift around 730 $cm^{-1}$ does not appear to depend on the oxidation state of the dopant, as indicated by the absence of any peak shifts for 10Pr and 10Tb. Neither is a correlation with the Ce-O bond length likely, because the corresponding Raman shifts around 730 $cm^{-1}$ do not correlate with the trends derived from the PXRD patterns (Figures S3-S4).

Reduction of ceria at higher temperatures (above 873 K) was reported to lead to the appearance of a wide band from 3500 to 1000 $cm^{-1}$ with a maximum around 2500 $cm^{-1}$ which originates either from semiconductor properties or from the formation of bulk defects (oxygen vacancies or $Ce^{3+}$).[5] In the present series, the intensity of this band does not seem to be linked to the $Ce^{3+}$ content, because it is strongest in 10Pr and 10Tb, while the $Ce^{3+}$ content in these samples decreases (cf. XANES data in Figure 11 in the main text). 10Cr displays lower intensity despite higher $Ce^{3+}$ contents (cf. Figure 11). In 10V and 10Nb (the only two samples with pentavalent dopants and therefore n-semiconductors) this band is also weakened with increasing $Ce^{3+}$ content. Assuming that the band arises from oxygen vacancies instead of $Ce^{3+}$, it is possible that these vacancies are mainly associated with the reduced dopant. This is in line with 10Pr and 10Tb undergoing reduction from +IV to +III (see below) while displaying the highest band intensity in the respective region. In contrast, Hf and Zr display stable oxidation states of +IV along with little changes in the 3000 to 1000 $cm^{-1}$ region. The spectroscopic results thus suggest the presence of two types of oxygen vacancies. The first type then arises from overall charge compensation, while the second type is due to thermochemical ceria reduction.

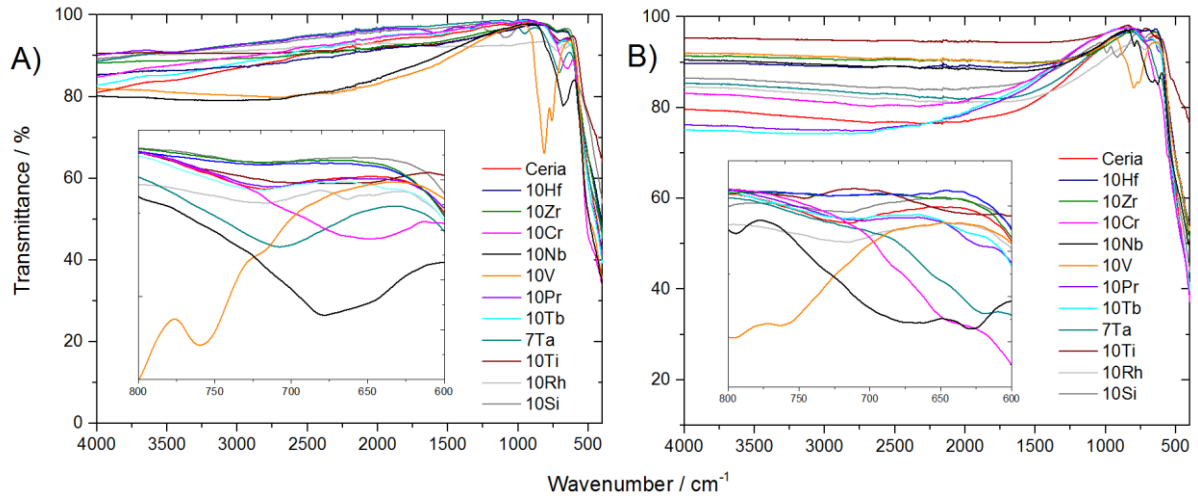


**Figure S8.** FT-IR spectra of doped ceria before (a) and after (b) TGA.

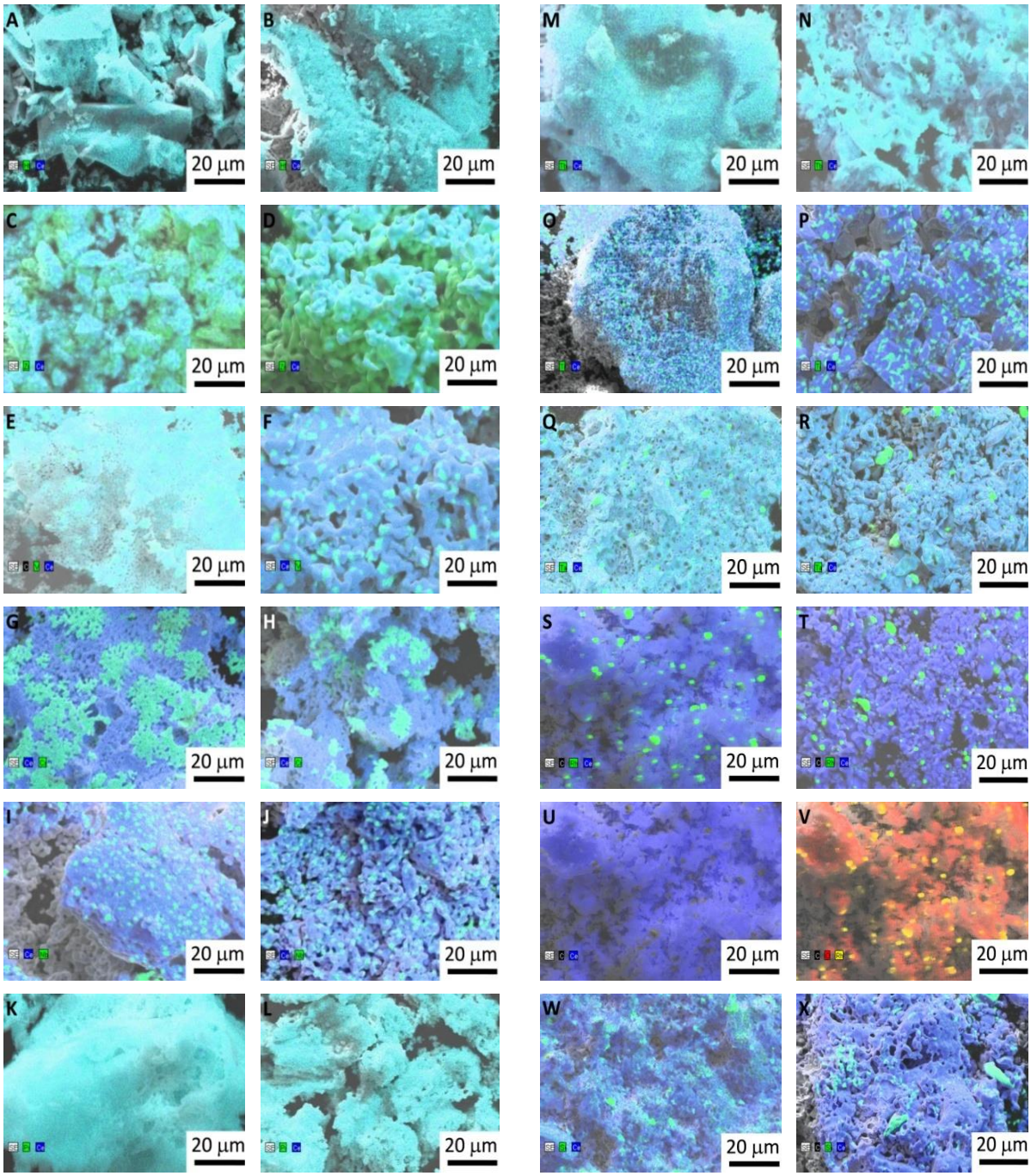


**Figure S9.** SEM/EDX mapping (1000x magnification) before (left) and after TGA (right) of 10Hf (a, b), 10Zr (c, d), 10V (e, f), 10Cr (g, h), 10Nb (i, j), 10Pr (k, l), 10Tb (m, n), 10Ti (o, p), 7Ta (q, r), 10Rh (s, t), 10Rh before TGA with Ce mapped (u) as well O and Rh mapping (v), and 10Si (w, x).

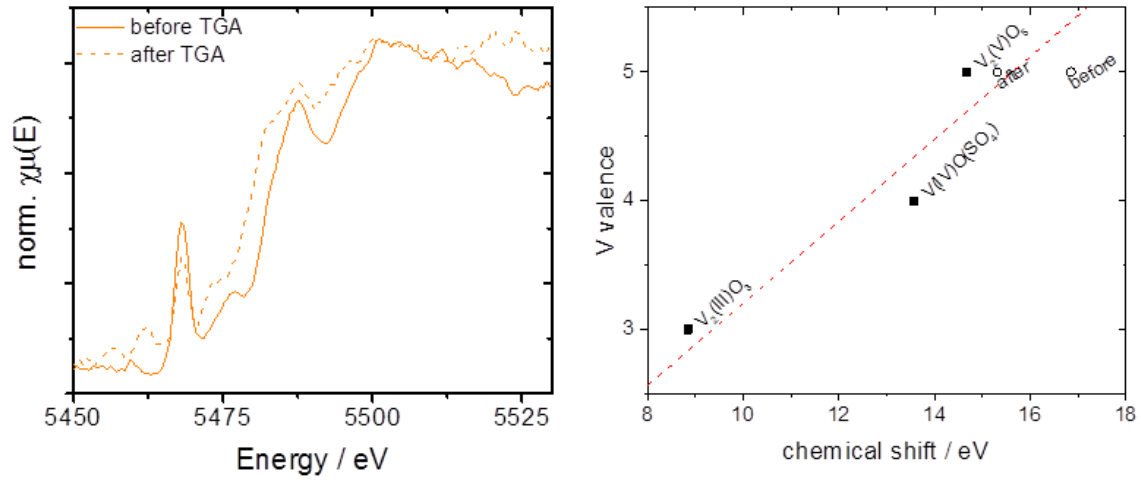


**Figure S10.** Left: K-edge XANES for 10V before and after TGA (left); right: edge position vs. valence state of selected reference standard (black squares) and 10V before and after TGA (open circles).

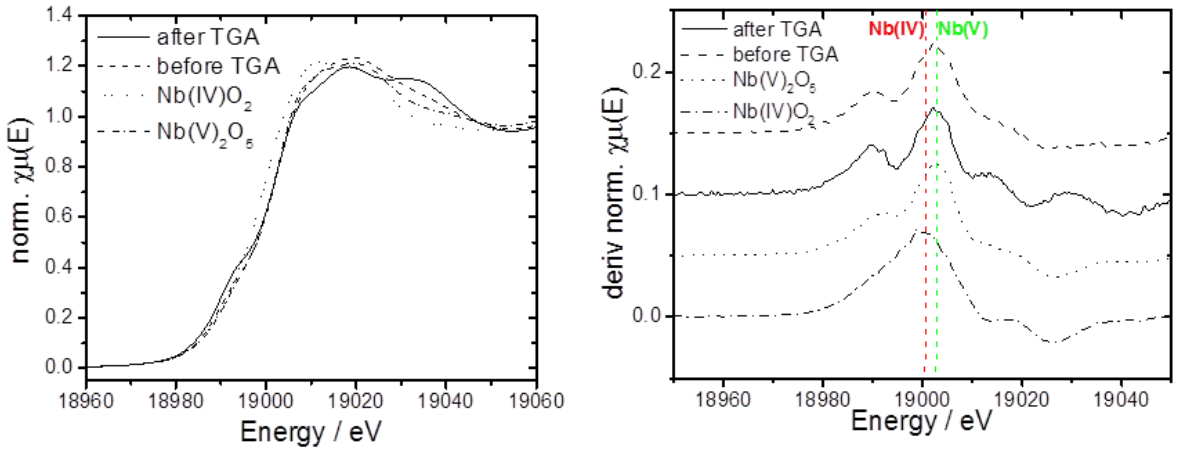


**Figure S11.** Left: Nb K-edge XANES of 10Nb before and after TGA vs. $Nb(IV)O_2$ and $Nb(V)_2O_5$ as references; right: first derivative plots of the K-edge spectra of 10Nb and of the references.

**Table S1.** Summary of the experimentally determined oxygen exchange capacity, $\Delta\delta$, determined for the synthesized materials compositions as indicated (with ceria reduction at 1500°C and 1 bar Ar, and ceria oxidation at 1000°C and 0.5 bar $CO_2$ in Ar).

| Synthesized composition | Δδ / wt.% | Modeled composition | $q_D$ / e | $q_O$ / e | $d_{Ce\text{-}O}$ / Å |
|---|---|---|---|---|---|
| $CeO_2$ | 0.053 ± 0.075 | $CeO_2$ | 2.42 | -1.20 | 4.52 |
| $Ti_{0.1}Ce_{0.9}O_2$ | 0.47 ± 0.031 | $Ti_{0.25}Ce_{0.75}O_2$ | 2.13 | -1.15 | 4.95 |
| $V_{0.1}Ce_{0.9}O_2$ | 0.38 ± 0.013 | $V_{0.25}Ce_{0.75}O_2$ | 2.03 | -1.12 | 6.66 |
| $Cr_{0.1}Ce_{0.9}O_2$ | 0.47 ± 0.056 | $Cr_{0.25}Ce_{0.75}O_2$ | 1.74 | -1.07 | 6.62 |
| $Zr_{0.1}Ce_{0.9}O_2$ | 0.59 ± 0.014 | $Zr_{0.25}Ce_{0.75}O_2$ | 2.53 | -1.24 | 4.54 |
| $Nb_{0.1}Ce_{0.9}O_2$ | 0.56 ± 0.003 | $Nb_{0.25}Ce_{0.75}O_2$ | 2.60 | -1.19 | 5.10 |
| $Pr_{0.1}Ce_{0.9}O_2$ | 0.46 ± 0.019 | | | | |
| $Tb_{0.1}Ce_{0.9}O_2$ | 0.43 ± 0.187 | | | | |
| $Hf_{0.1}Ce_{0.9}O_2$ | 0.65 ± 0.005 | $Hf_{0.25}Ce_{0.75}O_2$ | 2.60 | -1.25 | 4.56 |
| $Ta_{0.07}Ce_{0.93}O_2$ | 0.62 ± 0.000 | $Ta_{0.25}Ce_{0.75}O_2$ | 2.75 | -1.22 | 4.93 |

Errors are one standard deviation. This data is given with the (ideal-oxidized) stoichiometry of the DFT model representing a specific synthesized material, followed by DFT-computed partial electronic charge (in units of the elementary charge, e) of the metal cation dopant, $q_D$, the partial electronic charge of the oxygen anion, $q_O$, and (C) the shortest bonding length between the Ce cations and the O anions that form oxygen vacancies, $d_{Ce\text{-}O}$ (in Å).

## References


[1] M. Mogensen, N.M. Sammes, G.A. Tompset, *Solid State Ionics*, 2000, **129**, 63-94.
[2] http://jana.fzu.cz
[3] B.H. Toby, *Powder Diffr.*, 2006, **21**, 1, 67-70.
[4] M. Guo, J. Lu, Y. Wu, Y. Wang, M. Luo, *Langmuir*, 2011, **27,** 3872-3877.
[5] G. Rao, H. Sahu, *Proc. Indian Acad. Sci. (Chem. Sci.)*, 2001, **113,** 651-658.
[6] C. Binet, M. Daturi, J.-C. Lavalley, *Catal. Today*, 1999, **50,** 207-225.
[7] J. Scheffe, R. Jacot, G.R. Patzke, A. Steinfeld, *J. Phys. Chem. C*, 2013, **177**, 24104-24114.